Broadband photoluminescence of epitaxial bismuth nanowires and planar nanostructures

Andrey K. Kaveev[1,2,*], Vladimir V. Fedorov[1,3], Alexander Pavlov[1,3], Dmitry V. Miniv[1], Demid A. Kirilenko[4], Dmitrii A. Pudikov[4], Mikhail I. Vexler[2], Alexandr S. Goltaev[1], Sergey D. Komarov[5], Alexey M. Nadtochiy[5], Natalia V. Kryzhanovskaya[5] and Ivan S. Mukhin[1,3]

[1] Alferov University, St. Petersburg, 195220, Russian Federation

[2] Ioffe Institute, St. Petersburg, 194021, Russian Federation

[3] Peter the Great St. Petersburg Polytechnic University, St. Petersburg, 195251, Russian Federation

[4] St. Petersburg State University, St. Petersburg, 199034, Russian Federation

[5] HSE University, St. Petersburg, 194000, Russian Federation

*Correspondence email: kaveevandrei@yandex.ru

Abstract

Bismuth nanostructures represent a promising material platform for semiconductor nanooptoelectronics and colorimetry owing to the multi-colored light reflection and quantum confinement. In this work, we study photoluminescent properties of bismuth nanostructures grown using molecular beam epitaxy on the planar CaF_2/Si(111) surface. We demonstrate different surface morphology of Bi, from planar films obtained at a low growth temperature to island nano-arrays at elevated temperatures. The formation of individual bismuth nanowires is also demonstrated. Broadband photoluminescence of bismuth in the visible spectral range is revealed both for planar layers and nano-island arrays, as well as nanowires. The role of Bi^{3+} ions in photoluminescence was excluded by covering Bi nanostructures with epitaxial CaF_2 capping layer preventing bismuth from ambient humidity and oxidation. According to the performed density functional theory calculations, the nature of broadband photoluminescence is associated with interband transitions, accompanied by intraband phonons scattering.

Keywords: bismuth, nano-arrays, nano-islands, nanowires, photoluminescence, DFT, interband and intraband transitions

1. Introduction

Bismuth is a V-group element, having a number of outstanding properties [1]. It is one of the heaviest non-radioactive elements, exhibiting strong spin-orbit interactions, resulting in significant spin splitting of surface states due to the Rashba effect [2]. The $6s^2$ configuration of the outer electron shell of bismuth is close to that of dielectrics. At the same time, bismuth electronic structure in bulk crystals is similar to a semi-metal due to the existing overlap between the valence band and conduction band, which leads to the appearance of semi-metallic properties. Thus, the density of free charge carriers is $3 \times 10^{17} cm^{-3}$, and their mean free path is 1 mm at 100 K. Bismuth has the lowest known effective carrier mass, $m_{eff} \sim 0.001\ m_0$ [3], which is essential for transistor applications. The energy band structure of bulk bismuth crystals, which determines its properties as a semimetal, is described, for example, in [4].

Bismuth is widely employed in photonics. In particular, the dependence of the spectral position of reflected light in a broad range of 300-1200 nm on the size of bismuth nanoparticles has been demonstrated [5,6]. This phenomenon is in demand in the development of devices with color selection based on color rendering effects. Moreover, bismuth possesses a negative real part of the permittivity [7]. This property is manifested in the surface plasmon resonance effects. The broadband switching of the optical parameters of bismuth-containing systems is demonstrated [7]. In particular, the possibility of controlling the absorption temperature in the ultraviolet (UV) range due to liquid-solid phase transitions in switchable plasmonic metamaterials was shown. Several reports present the photoluminescent (PL) properties of bismuth films in the spectral range of 400-800 nm [8,9]. PL response is usually associated with the inter-level transitions

in Bi^{3+} ions [9]. Thus, bismuth can be used to develop broadband nanophotonic devices. The work [10] reports a broadband (370-1550 nm) detector based on planar bismuth films, in which the photocurrent passes through topologically protected surface states arising due to strong spin-orbit splitting. The authors of Ref. [11] describe a photodetector based on a bismuth-graphene system operating due to the photocurrent caused by the built-in field at the heterointerface. In nanoelectronics, it is suggested to move from planar layers to nanowire (NW) geometry for more efficient photogeneration of electron-hole pairs in quasi-one-dimensional systems [12,13]. A high electron mobility transistor based on bismuth NWs was presented in ref. [14], since m_{eff} of charge carriers in bismuth is extremely low. A number of reports discuss the strong anisotropy of the bismuth Fermi surface [15–17], as well as the quantum confinement effect in Bi NWs [18–20]. According to the performed calculations, this effect should lead to a semimetal-semiconductor transition in bismuth. The thermoelectric properties of bismuth NWs are described in ref. Notably, bismuth films [21–26] and NWs [27–30] can be epitaxially grown on various substrates, such as GaAs, silicon and glass.

In this work we study the PL properties of bismuth nanostructures with different morphologies (planar, nano-islands and NWs) grown on Si(111) substrates with the use of molecular beam epitaxy (MBE). MBE-grown CaF_2 layers are employed as buffer dielectric layers during the growth, as well as the capping layer covering Bi structures and protecting Bi from oxidation. The PL mechanism associated with intra-band transitions is discussed.

2. Results and discussion

2.1. Surface morphology and crystalline structure of Bi grown on CaF_2/Si(111)

The CaF_2 buffer layer was produced using two-stage growth of the material at a temperature of 250°C (first 15 monolayers) and 770°C (additional 20 monolayers) without material flux interruption during the temperature ramp from 580 to 770°C with characteristic growth rate about 1 nm/min. The detailed description of the employed CaF_2 staged growth approach is presented in [31]. Being deposited on the Si(111) substrate, calcium fluoride inherits the orientation of the main crystallographic axes, forming a planar surface [32]. The equivalent thickness of bismuth for all studied samples was 80-100 nm. Depending on the growth conditions, continuous bismuth films or, with an increase in temperature from room temperature to 150°C and above, ensembles of nano-islands were formed on the CaF_2(111) surface. Beginning from a temperature of about 100°C and above, along with the formation of islands, stochastic nucleation of long NWs with a diameter of around 70 nm and length of up to 10 μm occurred. Therefore, the growth temperature is a key factor governing the Bi nanostructure morphology. Additionally, to protect Bi nanostructures from oxidation, a part of the grown Bi samples was covered with a 10 nm thick capping layer of Bi grown at room temperature and growth rate of 1 nm/min. Details of the MBE growth are given in Materials and Methods section. Fig. 1 shows the typical scanning electron microscopy (SEM) images of the morphology of grown bismuth-based nanostructures. It should be noted that Bi nanowires nucleate on the island layer and grow on a planar layer and/or islands (not directly on a CaF_2 buffer layer), therefore it is impossible to obtain a sample containing only nanowires.

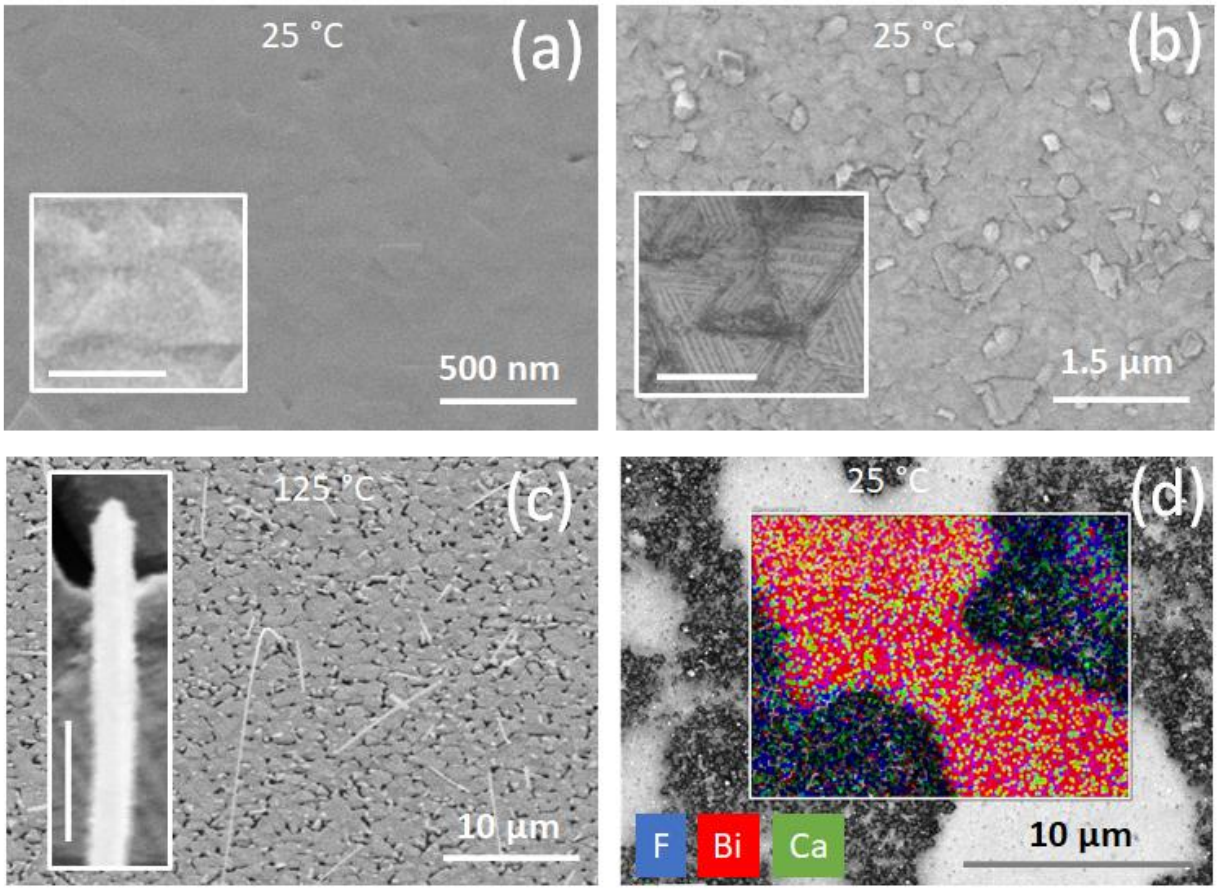

Fig. 1. Surface morphology of Bi-based nanostructures grown on Si(111) substrates using a CaF_2 buffer layer. (a) SEM image of a planar bismuth film grown at temperature of 25°C without a capping CaF_2 layer ($Bi/CaF_2/Si(111)$ system). (b) SEM image of $CaF_2/Bi/CaF_2/Si(111)$ system grown under similar conditions. The insets in (a) and (b) show areas of these samples in more detail, the scale bars correspond to 200 nm. (c) Stochastically formed NWs at an elevated bismuth growth temperature of 125°C and covered with a protecting CaF_2 layer deposited at room temperature. The surface represents a planar film with nucleated Bi nano-islands. The inset shows a single NW in more detail (scale bar corresponds to 200 nm). (d) EDX map of the boundary region of the sample shown in (b).

For a bismuth layer (Bi/CaF_2 buffer/Si(111) system) grown at temperatures below 100°C, the surface is relatively flat and smooth (see Fig. 1 (a)). The surface is almost completely planar. In the case of a planar bismuth layer grown at the same conditions, but additionally covered with a 10 nm thick CaF_2 capping layer at room temperature, the surface presents a corrugated morphology corresponding to the capping CaF_2 layer (see Fig. 1 (b)). The insets in Fig. 1(a) and (b) show the enlarged surface areas of these films. For the evaluated bismuth growth temperature (exceeding 100 °C), the formation of Bi NWs was revealed (see Fig. 1 (c)). This sample was also covered with a 5-10 nm capping CaF_2 layer at room temperature. The inset in Fig. 1(c) shows an individual NW tip in more detail. One can notice the corrugated nature of the NW surface, which is associated with the presence of the capping CaF_2 layer. To study a Bi and CaF_2 distribution, energy dispersive X-ray spectroscopy (SEM-EDX) measurements were performed on the boundary area, where the coverage with the bismuth film was incomplete (see Fig. 1(d), where the bright areas correspond to the Bi). It is evident that calcium and fluorine at`oms (corresponding to crimson and red colors) are presented on the entire surface sample, while bismuth atoms are found only in certain areas. To prove that a CaF_2 seen in the SEM-EDX corresponds not only to a buffer layer, but to a capping layer also, additional SEM cross-section measurements have been carried out (see Supplementary materials), and transmission electron microscopy (TEM) measurements were also performed (see Fig. 2 (e) and S2 in Supplementary materials). Additionally, our previous study [33] experimentally showed that the MBE-grown F-containing capping layer (CaF_2 and MoF_2) can fully protect metal surfaces (in particular,

cobalt) from oxidation, even being deposited at room temperature with a thickness as low as 5 nm. The reported in [33] XAS spectra showed its continuous, with no traces of metal oxide.

The performed X-ray diffraction (XRD) measurements (Fig. 2(a)) showed that in all three cases the bismuth nanostructures form a rhombohedral crystal structure of the R$\bar{3}$mH space group, typical for bulk crystals. This structure can be represented in both the rhombohedral and hexagonal bases. A complex multidomain structure for both the planar layer and the array of nano-islands is demonstrated. It was shown that during the transition from planar film to island geometry, the growth plane changes the orientation from (001) to (012) (in the hexagonal representation). Fig. 2(a) shows the intensity distribution over the specular reflection (lower part of the figure) and the corresponding reciprocal space map in the region of this reflection (upper part of the figure) for the sample containing a planar Bi film and Bi nano-islands.

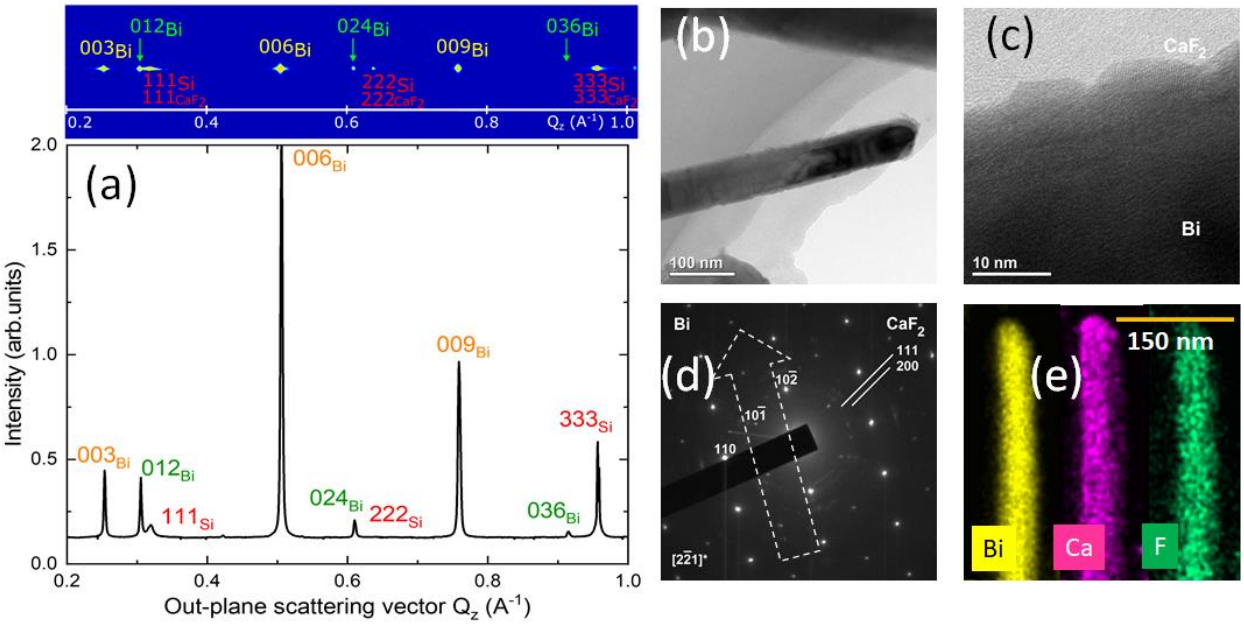

Fig. 2. (a) Intensity distribution profile over the specular reflection and the reciprocal space map in the region of this reflection. Red, green and orange colors mark reflections from the family of Si(111), Bi(012) and Bi(001) planes, respectively. (b) Bright-field TEM image of bismuth NWs. (c) HR-TEM image of the NW surface. (d) SAED pattern of the NW, the dashed arrow shows the orientation direction of the NW corresponding to the [110] growth direction. Strong Bi and weak CaF_2 reflection groups are marked by the text notations. (e) TEM-EDX images of Bi, Ca and F elements showing an uniform coverage of the NWs with calcium fluoride.

Several series of XRD reflections are clearly visible in Fig. 2a. The reflections corresponding to the (111) surface of Si and CaF_2 are shown in red, the reflections from the (012) and (001) planes of bismuth are shown in green and orange, respectively. It should be noted that the (001) plane set predominates for samples with a planar bismuth surface, while the (012) set is more pronounced for nano-island arrays.

TEM was applied to study the crystal structure of Bi NWs. Fig. 2(b-d) show the results of bright-field (BF-TEM) and selective area electron diffraction (TEM-SAED) measurements. The different grey zones, seen in Fig. 2(b), are related to specific crystalline features. The darker motley grey zone is related to a crystalline part of NW. A longitudinal color inhomogeneity may be attributed to a diffraction contrast related to probable thickness inhomogeneity and slight bending of NW. High resolution TEM (HR-TEM) images demonstrate a continuous polycrystalline CaF_2 layer covering the NW (Fig. 2 (c) and Fig. S2 in Supplementary materials) with an estimated thickness of 5-10 nm. Similarly, the thickness of the CaF_2 capping layer can be measured using cross-sectional SEM images (see Figure S3 of Supplementary materials), giving the same estimation. It is evident from the SAED pattern (Fig. 2(d)) that the NWs grow

along the [110] direction. The reflections corresponding to the polycrystalline CaF_2 layer are also distinguishable. To prove the formation of a capping CaF_2 layer on the NW surface, measured TEM-EDX maps are shown in Fig. 2 (e). It is clearly seen that CaF_2 completely covers the NW body, and both Ca and F atoms are uniformly distributed over the entire surface of the Bi nanocrystal. A more detailed description of the growth modes of Bi/CaF_2/Si(111) nanostructures not covered by a calcium fluoride capping layer can be found in [34]. Generally, high crystalline quality of NWs was confirmed by HR-TEM, which is shown in Fig. S1 of Supplementary materials.

Finally, we carried out X-ray photoelectron spectroscopy (XPS) measurements. This direct analytical method shows the surface chemical composition, including the presence of oxides. The obtained results (see Fig. S9 in the Supplementary information) clearly show the peaks associated with Ca and F, as well as O and C always presented in all surfaces as adsorbates and contaminators. Strong signals corresponding to the Ca2p and F1s doublets are direct evidence of the presence of the capping layer. At the same time there are no pronounced peaks associated with Bi and Bi-O. As known, the surface-sensitive XPS provides the information about very surface of the studied sample (3-5 nm depth). It means that CaF_2 layer thickness exceeds this value (about 5-10 nm according to the used growth regime) and this layer is continuous. Thus, a CaF_2 layer efficiently covers the Bi nanostructures preventing it from oxidation. The measurements were carried out at several points, and the results were identical.

2.2. Photoluminescence properties of Bi nanostructures

Previous studies of photoluminescence properties of Bi films, reported in [8], associate the optical response with radiative transitions in Bi ions. These ions appear due to the oxidation of the Bi structures. In our work, the Bi films and NWs were covered with a capping CaF_2 layer, preventing the formation of Bi ions. PL of bismuth films, nano-islands, as well as NWs, was detected upon the excitation by a blue laser with a wavelength λ_L = 457 nm and a power of 0.09-0.93 mW. The excitation laser beam was focused onto the surface of the sample using a 100X objective lens, forming a spot with a diameter of approximately 0.5 μm in diameter. The optical pump power density in the spot was in the range of 46–474 kW/cm^2. The PL intensity (I) was high enough to record the spectrum with a signal-to-noise ratio of 3-5, using a grating monochromator, equipped with a 150/475 grating and the CCD matrix detector (Sol instruments HS 101H-2048/122-HR2). The optical signal was registered during multiple recordings. The collected radiation was characterized by a wide spectral distribution $dI/d\lambda$. Fig. 3 shows the PL spectra of bismuth nanostructures grown on silicon substrates ((a) and (b) – thin films and films with Bi islands, respectively; (c) – NWs separately transferred to an auxiliary quartz substrate). Note, the "wavelength" argument is converted to the more convenient "photon energy" argument (according to the formula $dI/d[\hbar\omega] = dI/d\lambda \cdot \lambda^2/(2\pi\hbar c)$, $[\hbar\omega] = 2\pi\hbar c/\lambda$, where c is the speed of light in vacuum, and $[\hbar\omega]_{eV} = 1240/\lambda_{nm}$ for simplicity). Although the spectra in Fig. 3 are mainly correspond to the visible spectral range, the optical response also covers the long-wave edge, corresponding to the near infrared region. On the contrary, for the short-wave boundary coincided with λ_L, at shorter wavelengths the intensity dropped sharply. The features near the short-wave edge of the spectrum are associated with the Raman bands. These bands represent the superposition of Si and quartz bands, since Bi Raman lies out of the range [8], shown in Fig. 3. No other pronounced features were observed. The spectra of the background illumination of the silicon and quartz substrates are also presented as references. It should be noted that the acquired spectra do not demonstrate the pronounced peaks close to 500 nm, which is ascribed in [8] to PL of Bi^{3+} ions. This proves the absence of ions in our samples and emphasize a CaF_2 capping layer protection role.

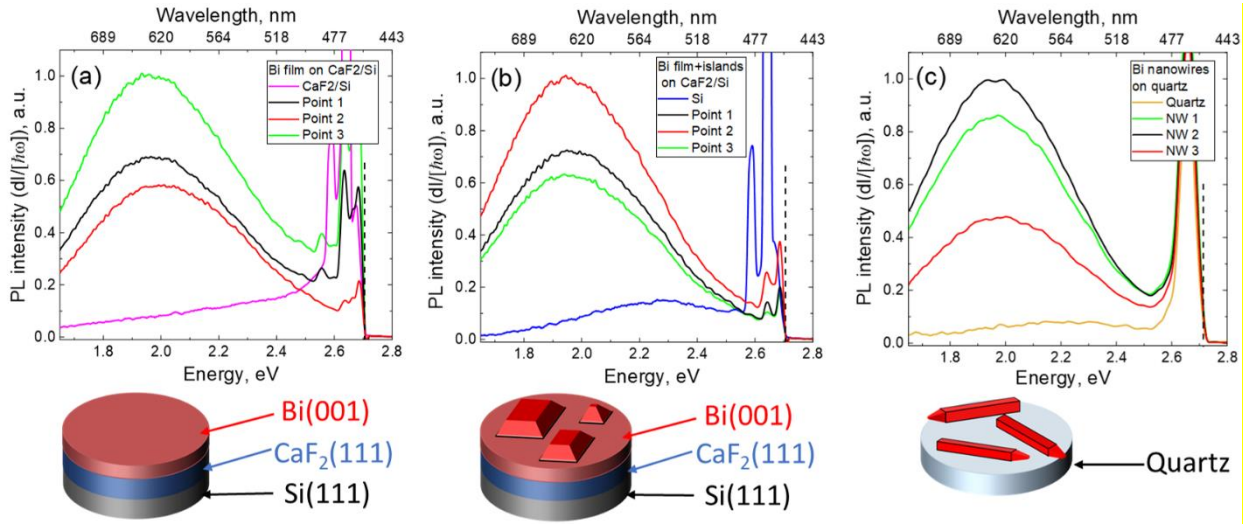

Fig. 3. Normalized to maximum differential PL spectra $dI/d[\hbar\omega] = dI/d\lambda \cdot \lambda^2/(2\pi\hbar c)$ of (a) thin bismuth films, (b) thin Bi films with nucleated Bi islands on CaF_2/Si substrates, and (c) separately transferred bismuth NWs onto a quartz substrate at different points. An excitation wavelength of 457 nm (2.71 eV) is marked with the dashed lines. The insets show corresponding schematic presentations of the Bi structures' morphology.

Measurements for each of the Bi-structure samples were performed at three different points, indicated as Point 1, 2 and 3. The measurements at different points were aimed to estimate the PL response homogeneity over the samples. One can see that the PL spectra correspond to each other and have the same spectral position of maxima and shapes. They only differ in intensity, which can be explained by the difference in the material volume excited under laser beam. This corresponds well to the SEM morphology study revealing the variation of Bi layer thickness (see Fig. S4). Thus, the observed results confirm the homogeneous and conformal covering the Bi structures by CaF_2 capping layers over the whole samples' surface. The estimated full width at half maximum (FWHM) values are 0.66-0.67, 0.68-0.69 and 0.60-0.61 eV for planar Bi film, nano-islands and NWs, respectively.

We should additionally note that no any correlation between morphology and PL spectral shape was observed. This correlation may appear via quantum-confinement effects. But quantum-confinement effects in Bi nanostructures become observable when the characteristic dimension is lower than ~50–70 nm at cryogenic temperatures [35–38]. This critical size decreases with temperature, reaching approximately 20–30 nm at room temperature [39,40]. In the current study we worked with Bi layers or islands having significantly larger dimensions (see the corresponding SEM and TEM images), therefore we do not expect any quantum-sized effects. It explains the independence of PL signals on the morphology of the studied structures.

The nature of the observed PL may be explained by interband electron transitions from different energy bands. We consider the possible transitions within the electronic band structure $E(\mathbf{k})$, where radiative transitions may occur either (i) between distinct bands (with or without electron-phonon interaction) or (ii) within a single band (requiring electron-phonon scattering). Some of these transitions are associated with photon emission. Under laser excitation (with energy $\hbar\omega_L$), electrons can unoccupy states above the Fermi level. These excited carriers subsequently relax via two primary pathways: (1) non-radiative energy dissipation through phonon scattering (dominant) or (2) radiative recombination, emitting photons. The latter process may occur from any intermediate states in the bands above the Fermi level, yielding photons with energies $\leq\hbar\omega_L$. This broad emission spectrum can be observed because electrons can undergo partial phonon-mediated energy loss within the unoccupied states prior to radiative decay, facilitating both intraband and interband optical transitions. To better assess the probability of radiative recombination processes, we computed the electronic structure of bulk bismuth in its rhombohedral

structural phase using density functional theory (DFT). First, we optimized the geometric parameters of the structure, obtaining the lattice constant a_{rho}=4.734 Å and angle α_{rho}=57.691°, which agree well with experimental values [41,42]. Next, we calculated the electronic structure of the system using the TB09 (mBJ) exchange-correlation potential [43]. The calculated band structure is shown in Fig. 4(a). The employed approach yields a direct band gap (E_g) value of 40 meV at the L-point and an indirect band gap (E_0) value of -31 meV between the T- and L-points. These results demonstrate that the TB09 method provides significantly improved accuracy for electronic structure calculations compared to standard LDA or GGA methods, approaching the precision of more computationally intensive quasiparticle GW methods [44].

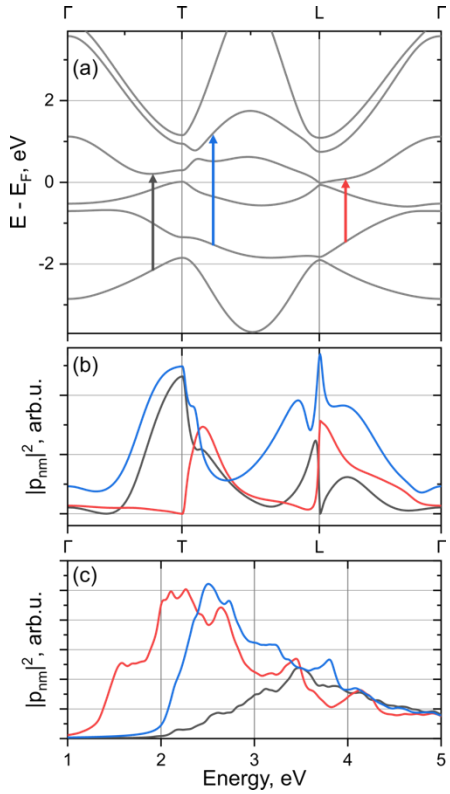

Fig. 4. (a) Band structure E(k) of bulk Bi calculated using the mGGA-TB09 exchange-correlation potential. Red, blue and black arrows indicate the optical transitions involved in momentum matrix element calculations. (b) Squared momentum matrix element $|p_{nm}(k)|^2$ as a function of k. (c) The dependence of the squared momentum matrix element $|p_{nm}(k)|^2$ on the transition energy. Note: blue, red and black curves in (b) and (c) correspond to transitions between the correspondence bands in (a).

Then, we evaluated possible interband transitions near the Fermi level, with the wavelengths from the excitation at 457 nm to the near-infrared range, where Bi exhibits significant absorption. The relevant transitions, indicated by color-coded arrows in the band structure, are shown in Fig. 4(a). Within the dipole approximation, the transition probability P is proportional to the squared momentum matrix element ($P \propto |p_{nm}|^2$). Fig. 4(b) shows the direction-averaged and normalized $|p_{nm}(\mathbf{k})|^2$, revealing sharp peaks near the T and L high-symmetry points. This indicates a higher probability of interband transitions involving these states. To further compare the experimental results with our theoretical model, we calculated the momentum matrix element on a 4 times shifted 25×25×25 Monkhorst-Pack k-grid. This allowed us to plot the dependence of $|p_{nm}(\mathbf{k})|^2$ on the transition energy (see Fig. 4c). Note that the small oscillations on the spectra are due to finite k-point sampling. Analyzing Fig. 4b and c, the main spectrum of emission should correspond to (500-700) nm band, which correlates well with the experimentally observed PL range of 500–700 nm. It is worth noting that direct quantitative comparison between experimental data and our theoretical results is not possible, since our model relies only on simple dipole approximation and does not account for the electron-phonon interaction. Thus, theoretically predicted high energy transitions can be weakened by electron-phonon scattering. However, the performed DFT calculations can be used as a first qualitative estimate that supports the relevance of interband optical transition in bulk Bi.

The described mechanism of luminescence is quite exotic, but not unique. A similar behavior was previously reported for semiconductors [45,46]. This mechanism is weakly realized in metals due to nonradiative relaxation on free carriers [47]. However, bismuth is a semimetal with a relatively low density of free carriers $n \sim 10^{17}/cm^{-3}$ (see Ref. [48]), which is several orders of magnitude lower compared to metals. It should be noted the radiative transition does not necessarily begin from the upper state of the excited electron, since its energy may be firstly partially relaxed non-radiatively to lower states via phonon scattering.

The observed effect seems to be a very curious property of the studied Bi nanostructures. Due to its nature, the PL brightness is relatively low, however it can be enhanced by the Purcell effect. The proper choice of nanostructure sizes in the array can provide the optical resonances at wavelengths corresponding to the broadband PL emission. The presence of Mie resonances, the Purcell effect and surface plasmon resonances at different wavelengths in Bi films and nanoparticles make them attractive in colorimetry and photonics [5,6].

3. Conclusion

In this study, we have observed PL from epitaxial bismuth nanostructures, including thin films, nano-island arrays, and nanowires grown on CaF_2/Si(111) substrates. Comprehensive structural characterization reveals the crystalline quality of these nanostructures. Our findings demonstrate that PL response originates from the bismuth nanostructures themselves, with a negligible contribution from the substrate. By employing an *in situ* CaF_2 capping layer, we have prevented the Bi surface oxidation and the formation of Bi ions luminescent centers.

The performed DFT analysis attributes the observed PL to radiative interband transitions, while phonon mediated scattering explains the observed broad emission spectrum with moderate intensity. This phenomenon provide the broadband light emission in semimetal systems. These findings open new possibilities for developing bismuth-based photonic components while providing fundamental insights into light-matter interactions in semimetal systems.

Materials and methods

MBE growth. Bi/CaF_2 heterostructures were grown on Si(111) substrates by molecular beam epitaxy (MBE) using a Veeco GEN III system. Three-inch silicon substrates (with resistivity of 0.1-0.01 Ω·cm) were pre-cleaned using a modified Shiraki procedure followed by the formation of a thin surface oxide layer in a boiling solution of ammonia, hydrogen peroxide and water ($NH_4OH/H_2O_2/H_2O$; 1:1:3) [49,50]. The Bi and CaF_2 fluxes were provided using the effusion cells. Bayard-Alpert ion gauge was used to measure the beam equivalent pressure (BEP) of the Bi flux. This flux was maintained at the pressure around 7×10^{-8} Torr, corresponding to a planar layer growth rate of 90 nm/h. The CaF_2 growth rate was maintained at the value about 1 nm/min and calibrated by a SEM measurement of a CaF_2 layer cleavage. The substrate was continuously rotated during the growth at a speed of 5 rpm. The growth process was monitored *in-situ* using reflection high-energy electron diffraction (RHEED) technique. CaF_2 sub-layer on Si substrate was grown using a two stage method [31], where 15 monolayers of CaF_2 were grown at 200°C, and further 20 monolayers - at 770°C. As a result, flat CaF_2 with a relief height of up to 2 nm is formed. Samples with bismuth were covered with a capping CaF_2 layer, which completely excluded the oxidation of bismuth and, accordingly, the formation of an oxide containing bismuth ions capable to participate in PL.

X-ray diffraction analysis. X-ray diffraction reciprocal space map (XRD-RSM) analysis was carried out to characterize the crystal structure of the Bi/CaF_2 nanoheterostructures using a monocrystal X-ray diffractometer Bruker Kappa Apex II with an Incoatec IμS 1.0 Cu-Kα X-ray source (λ = 1.5418 Å) and 2D detector Apex CCD. A set of 2D X-ray diffraction images obtained by measuring ω-rocking (±10°) scans with the 0.1° angular step and 10 s exposure time was assembled into a single reciprocal space map to study the mirror Bragg reflections.

SEM measurements and TEM characterization. The morphology of the synthesized Bi nanostructures was investigated using scanning electron microscopy (SEM) with a Zeiss SUPRA 25 system (D-73446,

Oberkochen, Germany). The crystal structure and homogeneity of the nanowires were studied by transmission electron microscopy in both high-resolution (HR-TEM) and high-angle annular dark-field (HAADF-STEM) modes using a JEOL JEM-2100F (Tokyo, Japan) microscope operating at 200 kV. For TEM characterization, the nanowires were mechanically detached from the growth substrate and transferred onto a TEM grid.

Photoluminescence measurements. PL spectra were acquired using Confotec NR500 confocal optical system. Optical pumping was performed using a 457 nm solid-state laser (CW), focused into spot with a diameter of 0.5 μm using a Nikon CF Plan Apo 100x 0.95 EPI objective. PL signal from the sample was collected using the same objective. PL spectra were investigated with a SOL instruments MS 5004i monochromator with a 150 gr/mm grating and a SOL instruments HS 101H-2048/122-HR2 CCD camera. The measurements were done at room temperature. The measurements were performed both for planar films, nano-arrays of islands and NWs grown on CaF_2/Si(111) substrates and NWs transferred onto an auxiliary quartz substrate. The samples were cut into pieces using a scalpel. The sample dimensions were 1×1 cm^2 area and dictated by the requirements of the used setup. For PL measurements of the isolated NWs, the NWs were transferred onto an auxiliary quartz substrate by dry transfer method (the substrate with NWs was mechanically contacted with an auxiliary substrate and then shifted). The latter completely eliminated parasitic PL from the substrate.

DFT calculations. We performed density functional theory (DFT) calculations using the ABINIT software package [51,52]. All calculations were carried out using the projector-augmented wave (PAW) method [53] with JTH PAW containing 5 valence electrons [54] and including spin-orbit coupling self-consistently. For structural optimization, we employed the PBE+D3 van der Waals functional [55], which has been shown to accurately predict bismuth's crystal structure [56]. The electronic structure of the system was calculated using the TB09 (mBJ) exchange-correlation potential [43].

XPS measurements. The XPS measurements were conducted using the photoelectron spectrometer "Escalab 250Xi" with AlKα radiation (photon energy 1486.6 eV). Spectra were recorded in the constant pass energy mode at 50 eV, using XPS spot size of 650 μm. A total energy resolution of the experiment was about 0.3 eV. Investigations were carried out at room temperature in an ultrahigh vacuum of the order of $1x10^{-9}$ mbar. The combined ion-electronic charge compensation system was used to remove the sample charge.

Acknowledgements

This work was supported by the Ministry of Science and Higher Education of the Russian Federation (grant no. FSEG-2024-0017). μ-PL spectroscopy studies were supported in the framework of the Basic Research Program at the National Research University Higher School of Economics (HSE University). D.K. thanks the research grant of St. Petersburg State University (ID 129360164) for TEM measurements.

References

[1] M. Kanatzidis, H. Sun, S. Dehnen, Bismuth — The Magic Element, Inorg. Chem. 59 (2020) 3341–3343. https://doi.org/10.1021/acs.inorgchem.0c00222.

[2] A. Takayama, Anomalous Rashba Effect of Bi Thin Film Studied by Spin-Resolved ARPES, in: Modern Technologies for Creating the Thin-Film Systems and Coatings, IntechOpen, 2017. https://doi.org/10.5772/66278.

[3] S.B. Cronin, Y.-M. Lin, O. Rabin, M.R. Black, G. Dresselhaus, M.S. Dresselhaus, Electronic Properties of Bismuth Nanowires, MRS Online Proceedings Library 679 (2011) 24. https://doi.org/10.1557/PROC-679-B2.4.

[4] H. Jin, B. Wiendlocha, J.P. Heremans, P-type doping of elemental bismuth with indium, gallium and tin: a novel doping mechanism in solids, Energy Environ. Sci. 8 (2015) 2027–2040. https://doi.org/10.1039/C5EE01309G.

[5] Y.-P. Chen, C.-C. Lai, W.-S. Tsai, Full-color based on bismuth core-shell nanoparticles in one-step fabrication, Opt. Express, OE 28 (2020) 24511–24525. https://doi.org/10.1364/OE.398903.

[6] L. Zhu, Z. Li, Y. Tian, Lithography-Free Bismuth Metamaterials for Advanced Light Manipulation, Photonics 10 (2023) 602. https://doi.org/10.3390/photonics10050602.
[7] Y. Tian, J. Toudert, Nanobismuth: Fabrication, Optical, and Plasmonic Properties—Emerging Applications, Journal of Nanotechnology 2018 (2018) 1–23. https://doi.org/10.1155/2018/3250932.
[8] N. Hussain, T. Liang, Q. Zhang, T. Anwar, Y. Huang, J. Lang, K. Huang, H. Wu, Ultrathin Bi Nanosheets with Superior Photoluminescence, Small 13 (2017). https://doi.org/10.1002/smll.201701349.
[9] M.H. Huang, S. Mao, H. Feick, H. Yan, Y. Wu, H. Kind, E. Weber, R. Russo, P. Yang, Room-Temperature Ultraviolet Nanowire Nanolasers, Science (2001). https://doi.org/10.1126/science.1060367.
[10] J.D. Yao, J.M. Shao, G.W. Yang, Ultra-broadband and high-responsive photodetectors based on bismuth film at room temperature, Sci Rep 5 (2015) 12320. https://doi.org/10.1038/srep12320.
[11] T.E. Huber, T. Brower, S.D. Johnson, J.H. Belk, J.H. Hunt, Photocurrent in Bismuth Junctions with Graphene, (2017). https://doi.org/10.48550/arXiv.1709.05408.
[12] X. Duan, Y. Huang, Y. Cui, J. Wang, C.M. Lieber, Indium phosphide nanowires as building blocks for nanoscale electronic and optoelectronic devices, Nature 409 (2001) 66–69. https://doi.org/10.1038/35051047.
[13] Y. Cui, C.M. Lieber, Functional Nanoscale Electronic Devices Assembled Using Silicon Nanowire Building Blocks, Science (2001). https://doi.org/10.1126/science.291.5505.851.
[14] W. Shim, J. Ham, K. Lee, W.Y. Jeung, M. Johnson, W. Lee, On-Film Formation of Bi Nanowires with Extraordinary Electron Mobility, Nano Lett. 9 (2009) 18–22. https://doi.org/10.1021/nl8016829.
[15] Z. Zhang, X. Sun, M.S. Dresselhaus, J.Y. Ying, J. Heremans, Electronic transport properties of single-crystal bismuth nanowire arrays, Phys. Rev. B 61 (2000) 4850–4861. https://doi.org/10.1103/PhysRevB.61.4850.
[16] J. Heremans, C.M. Thrush, Y.-M. Lin, S. Cronin, Z. Zhang, M.S. Dresselhaus, J.F. Mansfield, Bismuth nanowire arrays: Synthesis and galvanomagnetic properties, Phys. Rev. B 61 (2000) 2921–2930. https://doi.org/10.1103/PhysRevB.61.2921.
[17] K. Liu, C.L. Chien, P.C. Searson, K. Yu-Zhang, Structural and magneto-transport properties of electrodeposited bismuth nanowires, Applied Physics Letters 73 (1998) 1436–1438. https://doi.org/10.1063/1.122378.
[18] H.H. Cheng, M.M. Alkaisi, S.E. Wu, C.P. Liu, FABRICATION OF BISMUTH NANOWIRE DEVICES USING FOCUSED ION BEAM MILLING, AIP Conference Proceedings (2009). https://www.academia.edu/867405/Fabrication_of_bismuth_nanowire_devices_using_focused_ion_beam_milling (accessed September 19, 2024).
[19] X. Sun, Z. Zhang, G. Dresselhaus, M.S. Dresselhaus, J.Y. Ying, G. Chen, Theoretical Modeling of Thermoelectricity in Bi Nanowires, MRS Online Proceedings Library (OPL) 545 (1998) 87. https://doi.org/10.1557/PROC-545-87.
[20] D.S. Choi, A.A. Balandin, M.S. Leung, G.W. Stupian, N. Presser, S.W. Chung, J.R. Heath, A. Khitun, K.L. Wang, Transport study of a single bismuth nanowire fabricated by the silver and silicon nanowire shadow masks, Applied Physics Letters 89 (2006) 141503. https://doi.org/10.1063/1.2357847.
[21] C. Chou, B.-X. Wu, H.-H. Lin, Structural properties of Bi thin film grown on Si (111) by quasi-van der Waals epitaxy, Sci Rep 12 (2022) 2764. https://doi.org/10.1038/s41598-022-06472-5.
[22] S. Hatta, Y. Ohtsubo, S. Miyamoto, H. Okuyama, T. Aruga, Epitaxial growth of Bi thin films on Ge(111), Applied Surface Science 256 (2009) 1252–1256. https://doi.org/10.1016/j.apsusc.2009.05.079.
[23] M. Plaza, M. Abuín, A. Mascaraque, M.A. González-Barrio, L. Pérez, Epitaxial growth of Bi ultra-thin films on GaAs by electrodeposition, Materials Chemistry and Physics 134 (2012) 523–530. https://doi.org/10.1016/j.matchemphys.2012.03.027.
[24] G. Jnawali, H. Hattab, C.A. Bobisch, A. Bernhart, E. Zubkov, C. Deiter, T. Weisemoeller, F. Bertram, J. Wollschläger, R. Möller, M.H. Hoegen, Epitaxial Growth of Bi(111) on Si(001), E-Journal of Surface Science and Nanotechnology 7 (2009) 441–447. https://doi.org/10.1380/ejssnt.2009.441.

[25] A.R. Jalil, X. Hou, P. Schüffelgen, J.H. Bae, E. Neumann, G. Mussler, L. Plucinski, D. Grützmacher, Phase-Selective Epitaxy of Trigonal and Orthorhombic Bismuth Thin Films on Si (111), Nanomaterials 13 (2023) 2143. https://doi.org/10.3390/nano13142143.
[26] S. Xiao, D. Wei, X. Jin, Bi(111) Thin Film with Insulating Interior but Metallic Surfaces, Phys. Rev. Lett. 109 (2012) 166805. https://doi.org/10.1103/PhysRevLett.109.166805.
[27] M. Kammler, M. Horn-von Hoegen, Low energy electron diffraction of epitaxial growth of bismuth on Si(111), Surface Science 576 (2005) 56–60. https://doi.org/10.1016/j.susc.2004.11.033.
[28] ye Tian, C. Guo, S. Guo, Y. Wang, J. Miao, Q. Wang, Q. Liu, Bismuth nanowire growth under low deposition rate and its ohmic contact free of interface damage, AIP Advances 2 (2012). https://doi.org/10.1063/1.3679086.
[29] S.A. Stanley, C. Stuttle, A.J. Caruana, M.D. Cropper, A.S.O. Walton, An investigation of the growth of bismuth whiskers and nanowires during physical vapour deposition, J. Phys. D: Appl. Phys. 45 (2012) 435304. https://doi.org/10.1088/0022-3727/45/43/435304.
[30] Y. Bisrat, Z.P. Luo, D. Davis, D. Lagoudas, Highly ordered uniform single-crystal Bi nanowires: fabrication and characterization, Nanotechnology 18 (2007) 395601. https://doi.org/10.1088/0957-4484/18/39/395601.
[31] N.S. Sokolov, S.M. Suturin, B.B. Krichevtsov, V.G. Dubrovskii, S.V. Gastev, N.V. Sibirev, D.A. Baranov, V.V. Fedorov, A.A. Sitnikova, A.V. Nashchekin, V.I. Sakharov, I.T. Serenkov, T. Shimada, T. Yanase, M. Tabuchi, Cobalt epitaxial nanoparticles on CaF2/Si(111): Growth process, morphology, crystal structure, and magnetic properties, Phys. Rev. B 87 (2013) 125407. https://doi.org/10.1103/PhysRevB.87.125407.
[32] C.A. Lucas, D. Loretto, G.C.L. Wong, Epitaxial growth mechanisms and structure of CaF2/Si(111), Phys. Rev. B 50 (1994) 14340–14353. https://doi.org/10.1103/PhysRevB.50.14340.
[33] S.M. Suturin, V.V. Fedorov, A.G. Banshchikov, D.A. Baranov, K.V. Koshmak, P. Torelli, J. Fujii, G. Panaccione, K. Amemiya, M. Sakamaki, T. Nakamura, M. Tabuchi, L. Pasquali, N.S. Sokolov, Proximity effects and exchange bias in Co/MnF2(111) heterostructures studied by x-ray magnetic circular dichroism, J. Phys.: Condens. Matter 25 (2012) 046002. https://doi.org/10.1088/0953-8984/25/4/046002.
[34] A. Kaveev, V. Fedorov, D. Miniv, A. Goltaev, D. Kirilenko, A. Malenin, I. Mukhin, Epitaxial growth of bismuth on CaF2/Si(111): from planar films to self-organized arrays of nanostructures, J Appl Cryst 58 (2025) 419–428. https://doi.org/10.1107/S1600576725001591.
[35] O. Prakash, A. Kumar, A. Thamizhavel, S. Ramakrishnan, Evidence for bulk superconductivity in pure bismuth single crystals at ambient pressure, Science 355 (2017) 52–55. https://doi.org/10.1126/science.aaf8227.
[36] D. Lükermann, S. Sologub, H. Pfnür, C. Tegenkamp, Sensing surface states of Bi films by magnetotransport, Phys. Rev. B 83 (2011) 245425. https://doi.org/10.1103/PhysRevB.83.245425.
[37] E. Sedov, K. Riikonen, K. Arutyunov, Quantum size effect in single-crystalline bismuth nanorods, Journal of Physics: Conference Series 929 (2017) 012088. https://doi.org/10.1088/1742-6596/929/1/012088.
[38] D. Martínez Lara, R. González-Campuzano, D. Mendoza, Quantum confinement effect in thin bismuth films: In search of the critical thickness for the semimetal–semiconductor transition, Thin Solid Films 821 (2025) 140678. https://doi.org/10.1016/j.tsf.2025.140678.
[39] C. E, N. A, Quantum size effect in the resistivity of bismuth nanowires, Solid State Communications 150 (2010) 118–121.
[40] T. Cornelius, M.E. Toimil-Molares, R. Neumann, G. Fahsold, R. Lovrincic, A. Pucci, S. Karim, Quantum size effects manifest in infrared spectra of single bismuth nanowires, Applied Physics Letters 88 (2006) 103114–103114. https://doi.org/10.1063/1.2183823.
[41] P. Cucka, C.S. Barrett, The crystal structure of Bi and of solid solutions of Pb, Sn, Sb and Te in Bi, Acta Cryst 15 (1962) 865–872. https://doi.org/10.1107/S0365110X62002297.
[42] Z. Wei, C. Dubceac, M.A. Petrukhina, E.V. Dikarev, From a volatile molecular precursor to twin-free single crystals of bismuth, Chem. Commun. 55 (2019) 5717–5719. https://doi.org/10.1039/C9CC02820J.

[43] F. Tran, P. Blaha, Accurate Band Gaps of Semiconductors and Insulators with a Semilocal Exchange-Correlation Potential, Phys. Rev. Lett. 102 (2009) 226401. https://doi.org/10.1103/PhysRevLett.102.226401.
[44] I. Aguilera, C. Friedrich, S. Blügel, Electronic phase transitions of bismuth under strain from relativistic self-consistent GW calculations, Phys. Rev. B 91 (2015) 125129. https://doi.org/10.1103/PhysRevB.91.125129.
[45] P.D. Yoder, M.I. Vexler, A.F. Shulekin, N. Asli, S.V. Gastev, I.V. Grekhov, P. Seegebrecht, S.E. Tyaginov, H. Zimmermann, Luminescence spectra of an Al⁄SiO2⁄p-Si tunnel metal-oxide-semiconductor structure, Journal of Applied Physics 98 (2005) 083511. https://doi.org/10.1063/1.2099507.
[46] J. Bude, N. Sano, A. Yoshii, Hot-carrier luminescence in Si, Phys. Rev. B 45 (1992) 5848–5856. https://doi.org/10.1103/PhysRevB.45.5848.
[47] A. Loirette-Pelous, J.-J. Greffet, Theory of Photoluminescence by Metallic Structures, ACS Nano 18 (2024) 31823–31833. https://doi.org/10.1021/acsnano.4c07637.
[48] G.A. Williams, Alfv\'en-Wave Propagation in Solid-State Plasmas. I. Bismuth, Phys. Rev. 139 (1965) A771–A778. https://doi.org/10.1103/PhysRev.139.A771.
[49] A. Ishizaka, Y. Shiraki, Low Temperature Surface Cleaning of Silicon and Its Application to Silicon MBE, J. Electrochem. Soc. 133 (1986) 666. https://doi.org/10.1149/1.2108651.
[50] W. Kern, The Evolution of Silicon Wafer Cleaning Technology, J. Electrochem. Soc. 137 (1990) 1887. https://doi.org/10.1149/1.2086825.
[51] X. Gonze, B. Amadon, G. Antonius, F. Arnardi, L. Baguet, J.-M. Beuken, J. Bieder, F. Bottin, J. Bouchet, E. Bousquet, N. Brouwer, F. Bruneval, G. Brunin, T. Cavignac, J.-B. Charraud, W. Chen, M. Côté, S. Cottenier, J. Denier, G. Geneste, P. Ghosez, M. Giantomassi, Y. Gillet, O. Gingras, D.R. Hamann, G. Hautier, X. He, N. Helbig, N. Holzwarth, Y. Jia, F. Jollet, W. Lafargue-Dit-Hauret, K. Lejaeghere, M.A.L. Marques, A. Martin, C. Martins, H.P.C. Miranda, F. Naccarato, K. Persson, G. Petretto, V. Planes, Y. Pouillon, S. Prokhorenko, F. Ricci, G.-M. Rignanese, A.H. Romero, M.M. Schmitt, M. Torrent, M.J. van Setten, B. Van Troeye, M.J. Verstraete, G. Zérah, J.W. Zwanziger, The ABINIT project: Impact, environment and recent developments, Computer Physics Communications 248 (2020) 107042. https://doi.org/10.1016/j.cpc.2019.107042.
[52] A.H. Romero, D. Allan, B. Amadon, G. Antonius, T. Applencourt, L. Baguet, J. Bieder, F. Bottin, J. Bouchet, E. Bousquet, F. Bruneval, G. Brunin, D. Caliste, M. Côté, J. Denier, C. Dreyer, P. Ghosez, M. Giantomassi, Y. Gillet, X. Gonze, ABINIT: Overview and focus on selected capabilities, The Journal of Chemical Physics 152 (2020) 124102. https://doi.org/10.1063/1.5144261.
[53] M. Torrent, F. Jollet, F. Bottin, G. Zérah, X. Gonze, Implementation of the projector augmented-wave method in the ABINIT code: Application to the study of iron under pressure, Computational Materials Science 42 (2008) 337–351. https://doi.org/10.1016/j.commatsci.2007.07.020.
[54] F. Jollet, M. Torrent, N. Holzwarth, Generation of Projector Augmented-Wave atomic data: A 71 element validated table in the XML format, Computer Physics Communications 185 (2014) 1246–1254. https://doi.org/10.1016/j.cpc.2013.12.023.
[55] B. Van Troeye, M. Torrent, X. Gonze, Interatomic force constants including the DFT-D dispersion contribution, Phys. Rev. B 93 (2016) 144304. https://doi.org/10.1103/PhysRevB.93.144304.
[56] V.I. Ushanov, S.V. Eremeev, V.M. Silkin, V.V. Chaldyshev, Plasmon Resonance in a System of Bi Nanoparticles Embedded into (Al,Ga)As Matrix, Nanomaterials 14 (2024) 109. https://doi.org/10.3390/nano14010109.